jove

Flapping Soft Fin Deformation Modeling using Planar Laser-Induced Fluorescence Imaging

Kaushik Sampath[*,1], **Nicole Xu**[*,2], **Jason Geder**[2], **Marius Pruessner**[3], **Ravi Ramamurti**[2]

[1] KS Research Inc [2] Laboratories for Computational Physics and Fluid Dynamics, US Naval Research Laboratory [3] Center for Biomolecular Science and Engineering, US Naval Research Laboratory

[*] These authors contributed equally

Corresponding Author

Jason Geder

jason.geder@nrl.navy.mil

Abstract

Propulsive mechanisms inspired by the fins of various fish species have been increasingly researched, given their potential for improved maneuvering and stealth capabilities in unmanned vehicle systems. Soft materials used in the membranes of these fin mechanisms have proven effective at increasing thrust and efficiency compared with more rigid structures, but it is essential to measure and model the deformations in these soft membranes accurately. This study presents a workflow for characterizing the time-dependent shape deformation of flexible underwater flapping fins using planar laser-induced fluorescence (PLIF). Pigmented polydimethylsiloxane fin membranes with varying stiffnesses (0.38 MPa and 0.82 MPa) are fabricated and mounted to an assembly for actuation in two degrees of freedom: pitch and roll. PLIF images are acquired across a range of spanwise planes, processed to obtain fin deformation profiles, and combined to reconstruct time-varying 3D deformed fin shapes. The data are then used to provide high-fidelity validation for fluid-structure interaction simulations and improve the understanding of the performance of these complex propulsion systems.

Introduction

In nature, many fish species have evolved to use a variety of body and fin motions to achieve locomotion. Research to identify the principles of fish locomotion has helped drive the design of bioinspired propulsion systems, as biologists and engineers have worked together to develop capable next-generation propulsion and control mechanisms for underwater vehicles. Various research groups have studied fin configurations, shapes, materials, stroke parameters, and surface curvature control techniques[1,2,3,4,5,6,7,8,9,10,11,12]. The importance of characterizing tip vortex generation and wake inclination to understand thrust generation in single- and multi-fin systems has been documented in numerous studies, both computational and experimental[13,14,15,16,17,18]. For fin mechanisms made of compliant materials, shown in various studies to reduce wake inclination and increase thrust[17],

it is also essential to capture and accurately model their deformation time-history to pair with the flow structure analysis. These results can then be used to validate computational models, inform fin design and control, and facilitate active research areas in unsteady hydrodynamic loading on flexible materials, which need validation[19]. Studies have used direct high-speed image-based shape tracking in shark fins and other complex objects[20,21,22], but the complex 3D fin shape often blocks optical access, making it difficult to measure. Thus, there is a pressing need for a simple and effective method to visualize flexible fin motion.

A material widely used in compliant fin mechanisms is polydimethylsiloxane (PDMS) due to its low cost, ease of use, ability to vary stiffness, and compatibility with underwater applications[23], as described extensively in a review by Majidi et al.[24]. In addition to these benefits, PDMS is also optically transparent, which is conducive to measurements using an optical diagnostic technique such as planar laser-induced fluorescence (PLIF). Traditionally within experimental fluid mechanics[25], PLIF has been used to visualize fluid flows by seeding the fluid with dye or suspended particles or taking advantage of quantum transitions from species already in the flow that fluoresce when exposed to a laser sheet[26,27,28,29]. This well-established technique has been used to study fundamental fluid dynamics, combustion, and ocean dynamics[26,30,31,32,33].

In the present study, PLIF is used to obtain spatiotemporally resolved measurements of shape deformation in flexible fish-inspired robotic fins. Instead of seeding the fluid with dye, the underwater kinematics of a PDMS fin are visualized at various chordwise cross-sections. Although planar laser imaging can be performed on regular cast PDMS without additional fluorescence, modifying PDMS to enhance fluorescence can improve the signal-to-noise ratio (SNR) of the images by reducing the effects of background elements, such as the fin mounting hardware. PDMS can be made fluorescent by employing two methods, either by fluorescent particle seeding or pigmentation. It has been reported that, for a given part ratio, the former alters the stiffness of the resultant cast PDMS[34]. Therefore, a nontoxic, commercially available pigment was mixed with transparent PDMS to cast fluorescent fins for the PLIF experiments.

To provide an example of using these fin kinematics measurements for computational model validation, the experimental kinematics are then compared with values from the coupled fluid-structure interaction (FSI) models of the fin. The FSI models used in the computations are based on the first seven eigenmodes computed using the measured material properties for the fins. Successful comparisons validate fin models and provide confidence in using the computational results for fin design and control. Further, the PLIF results demonstrate that this method can be used to validate other numerical models in future studies. Additional information about these FSI models can be found in prior work[35,36] and in fundamental texts of computational fluid dynamics methods[37,38]. Future studies can also allow for simultaneous measurements of solid deformations and fluid flows for improved experimental studies of FSI in robotic fins, bioinspired soft robots, and other applications. Furthermore, because PDMS and other compatible elastomers are widely used in various fields, including sensors and medical devices, visualizing deformations in flexible solids using this technique can benefit a larger community of researchers in engineering, physics, biology, and medicine.

Protocol

1. Fin fabrication

1. Build a fin mold based on the desired shape design.

   1. Design and build a custom 3D-printed gloss-finished mold of fin shape (**Figure 1**). See STL files for fabricating the mold in **Supplementary Coding Files 1-4**.

   2. Insert structural elements into the mold, such as a 3D-printed rigid plastic leading-edge spar. See the STL file of the spar in **Supplementary Coding File 2**.

2. Mix PDMS (see **Table of Materials**) in the desired part ratio.

   1. Select the part ratio of base elastomer to curing agent (i.e., 10:1 or 20:1) to achieve higher or lower elastic modulus, respectively. Weigh the corresponding amounts of base and hardener.
   NOTE: Both 10:1 and 20:1 (elastomer to curing agent) were used in the present study.

   2. Measure the fluorescent pigment (see **Table of Materials**) such that the total mixture contains 0.1%-1% pigment by weight, depending on the desired brightness of pigmentation. Add the pigment to the PDMS blend.

   3. Pour the measured amounts of elastomer, hardener, and pigment into a planetary centrifugal mixer (mixing at 423 x *g* for 30 s and de-aerating at 465 x *g* for 30 s) and mix accordingly.

3. Cast the fin in the mold.

   1. Degas and pour the PDMS mixture into the mold for the fin. Place the mold into the oven at 70 °C for 45 min, and let it cure overnight at 37 °C.

   2. Once the curing is complete, remove the cast fin from the mold (**Figure 2**).

4. Perform tensile testing following the ASTM standard[39].

   1. For each fin cast in Step 1.3., cast one Type IV specimen using the same PDMS and pigment blend in a Type IV shaped mold using the previously described Steps 1.1.-1.3.
   NOTE: See the STL files to cast the Type IV specimen in **Supplementary Coding File 5** (mold shown in **Figure 1C**), and see **Figure 3** for examples of the Type IV samples tested.

   2. Clamp the test specimen into the tensile testing machine (see **Table of Materials**). Measure the initial length, width, and thickness (mm) of the narrow sample section.

   3. Subject the test specimen to tension in 5 mm increments, ensuring that the sample remains stretched in the elastic region only, not overstretched. Decrease the tension in 5 mm increments until the total sample displacement is 0 mm (original position). Record the lengths (mm) and forces (N) of the narrow section at each increment.

   4. To calculate the elastic modulus of the sample, plot the stress-strain curve and determine the best linear fit and R^2 value.

2. Experimental setup and trials

1. Mount the PLIF hardware (see **Table of Materials**) to a rectangular glass water tank (2.41 m x 0.76 m x 0.76 m).

1. Mount and use a pulsed laser system (see **Table of Materials**) to generate a planar light sheet intersecting the tank at its mid-plane at a specified frequency (30 Hz), as shown in **Figure 4**.

2. Mount and use a 4 MP charge-coupled device (CCD) camera equipped with a lens (35 mm) and a longpass fluorescence filter (560 nm) (see **Table of Materials**).

3. Calibrate the micrometer-to-pixel conversion by taking a single image from the CCD camera with a ruler placed in the laser sheet plane (**Figure 5**). Select two positions on the camera and divide the distance in micrometers by separating pixels. Ensure this micrometer-to-pixel ratio is small enough (sub-millimeter) for the application.

2. Synchronize the laser pulses and camera images with the flapping fin using trigger outputs from the fin software and signals from a delay generator and associated software (see **Table of Materials**) to coordinate the camera, laser heads, and fin motion. See **Supplementary Figure 1** for an example of the delay generator software interface settings.

   1. Set the laser system.
   NOTE: Ensure all laser safety measures are in accordance with institutional guidelines.

      1. Turn the laser system on by rotating the power key to the right to run the chiller that cools the laser heads. The fault light blinks until the system is ready to power the lasers. Do not press the power button that turns the lasers on until all laser modes are set correctly.

      2. Set the **Trigger Source** to **EXT LAMP/EXT Q-SW** (external lamp/external Q-switch).

      3. For both laser heads, set the laser energy to the desired level (i.e., approximately 60%-80% of the full power) and ensure that the Q-switch is turned on by pressing each **Q-switch** button.

      4. Turn the lasers on by pressing the **Power button**.
      NOTE: As the **Trigger Source** is set to **EXT LAMP/EXT Q-SW**, the laser heads are ready to fire, but only fire after the system receives an external trigger from the software.

   2. Set the camera.

      1. Plug in the power cables to the camera and ensure proper connections to the computer and software.

      2. Open the camera settings software and select the proper port.

         1. Under **Trigger > Settings**, set "Trigger in:" to **External** and "Mode:" to **Fast**.

         2. Under **Exposure**, set "Exposure Control" to **Off**.

      3. Open the camera capture software and select the proper camera card.

         1. Click on the **Grab Sequence** button.

         2. Click on the **Capture Settings** button, select TIFF images, select **Series of frames ...**, and select the desired file path, **6 Digit Number**, **Continuous**, and **Accept**.

         3. Click on **Start Capture**.
         NOTE: As the camera settings are set to an external trigger, the camera is ready to collect images but only captures

these images after the system receives an external trigger from the software.

3. Set the delay generator.

   1. Turn on the delay generator, and connect the External Gate Channel to the fin trigger, Channels A-D to the laser (A: laser head 1, B: Q-switch to laser 1, C: laser head 2, and D: Q-switch to laser 2), and Channel E to the camera.

   2. Open the delay generator software.

   3. Select the "Pulse Mode" to **Burst** and "System Resolution" to **4 ns**.

   4. Set the "Period (s)" to **0.033333352**.

   5. Set the "External Trigger/Gate Mode" to **Triggered**, "Threshold (V)" to **0.20**, and "Trigger Edge" as **Rising**.

   6. On **Channels > Ch A**, click on the **Enabled** checkbox. Set the "Delay (s)" to **0.000000004**, "Width (s)" to **0.005000000**, "Amplitude (V)" to **5.00**, "Channel Mode" to **Duty Cycle**, "Wait Count" to **0**, "Sync Source" to **T0**, "Polarity" to **Normal**, "Multiplexer" to **A**, "Duty Cycle On" to **1**, "Duty Cycle Off" to **1**, and "Gate Mode" to **Disabled**.

   7. On **Channels > Ch B**, click on the **Enabled** checkbox. Set the "Delay (s)" to **0.000138000**, "Width (s)" to **0.005000000**, "Amplitude (V)" to **5.00**, "Channel Mode" to **Duty Cycle**, "Wait Count" to **0**, "Sync Source" to **Ch A**, "Polarity" to **Normal**, "Multiplexer" to **B**, "Duty Cycle On" to **1**, "Duty Cycle Off" to **1**, and "Gate Mode" to **Disabled**.

   8. On **Channels > Ch C**, click on the **Enabled** checkbox. Set the "Delay (s)" to **0.033333304**, "Width (s)" to **0.005000000**, "Amplitude (V)" to **5.00**, "Channel Mode" to **Duty Cycle**, "Wait Count" to **0**, "Sync Source" to **Ch A**, "Polarity" to **Normal**, "Multiplexer" to **C**, "Duty Cycle On" to **1**, "Duty Cycle Off" to **1**, and "Gate Mode" to **Disabled**.

   9. On **Channels > Ch D**, click on the **Enabled** checkbox. Set the "Delay (s)" to **0.000138000**, "Width (s)" to **0.005000000**, "Amplitude (V)" to **5.00**, "Channel Mode" to **Duty Cycle**, "Wait Count" to **0**, "Sync Source" to **Ch C**, "Polarity" to **Normal**, "Multiplexer" to **D**, "Duty Cycle On" to **1**, "Duty Cycle Off" to **1**, and "Gate Mode" to **Disabled**.

   10. On **Channels > Ch E**, click on the **Enabled** checkbox. Set the "Delay (s)" to **0.000000004**, "Width (s)" to **0.005000000**, "Amplitude (V)" to **5.00**, "Channel Mode" to **Normal**, "Wait Count" to **0**, "Sync Source" to **T0**, "Polarity" to **Normal**, "Multiplexer" to **E**, and "Gate Mode" to **Disabled**.

3. Align the fin so the laser sheet passes through one chordwise section of the fin at a selected spanwise position and secure the fin platform with the mounting hardware.

4. Connect the power to the fin control hardware and fin motors (see **Table of Materials**) to begin fin flapping with the selected kinematics, and turn off all ambient lights.

5. Press **Run** in the delay generator software to begin the synchronized experiments and acquire images of the intersection of the laser sheet with the fin throughout

the stroke cycle. This needs to be conducted over 200+ stroke cycles.

6. Press **Stop** in the delay generator software and disconnect the fin from the power source.

7. Move the fin platform so the laser sheet crosses at a new spanwise position and perform experiments to acquire the images again. Repeat Steps 2.3.-2.6. for the number of desired measurements (eight different spanwise positions, as shown by the black dashed lines in **Figure 2A**).

8. Replace the fin with additional desired fin membranes (two fin stiffnesses, PDMS 10:1 and PDMS 20:1) and repeat the experiments.

3. Image analysis

1. For each experimental trial conducted in Step 2.4., locate the file where the images are stored and create a subfolder for each fin position or phase throughout the stroke cycle. Sort the image files into their corresponding subfolders.

2. For each fin phase subfolder, read the 200+ images as pixel-value arrays (imread.m). Sum the pixel-value arrays for all the images and divide by the number of images to generate a mean image. Write the image to a new file (imwrite.m). Repeat this step for each fin position throughout the stroke cycle (30 positions).

3. Perform a histogram enhancement on each mean image (imadjust.m) to extend the dynamic intensity range of the images to the full available range to improve the contrast between the fin and background.

4. Set the intensity thresholds and binarize each image to obtain a black-and-white image (imbinarize.m). The

resulting white shapes should correspond to pieces of the fin cross-section.

5. Extract all white objects (fin pieces) from the binary image (bwareafilt.m), and display the image (imshow.m). Create a trace of the binary image boundary for each image to obtain a 2D shape by selecting all the fin (white) pixels that touch the background (black) pixels (bwboundaries.m).

NOTE: Due to imposed fin kinematics, the view of the PLIF measured cross-section in some frames may be occluded by another part of the fin. In such cases, either there is no coherent fin shape apparent from the images, or only the leading edge (LE) remains visible (**Figure 6**).

6. Perform Steps 3.1.-3.5. for each fin cross-section.

4. Reconstruction of 3D deflection

1. Assuming that the LE position (at least closer to the stroke axis) in the flexible cases is the same as that of the LE in a rigid fin of the same shape, line the plane cuts along their LE for the same time-step, and compare with the results from the corresponding rigid fin shape.

2. Use a least-squares fit to approximate the resulting centerline shape of the fin cross-section for all plane cuts and reconstruct the 3D fin shape using a simplified convex-hull from these fitted profiles.

3. Compare the resulting fin shapes with 3D FSI models (generated from their centerlines) to showcase how this process can be used as high-fidelity validation.

   1. Generate a surface triangulation of the partially rigid nylon and partially flexible PDMS fin.

   2. Use a commercial structural dynamics software (see **Table of Materials**) to obtain the eigenmodes of the hybrid material.

1. Perform scaling studies to match the steady-state displacement obtained using uniform pressure differential on the fin surfaces.

2. Scale the modes to match the displacement obtained from the software.

3. With the proper scale factor, use the first few dominant modes (usually 7 or 8) employed in the coupled FSI solver to simulate the unsteady flow over the flexible fin.

    1. Treat the body as an embedded entity in a background mesh.
    NOTE: The coupled solver was validated for the Turek-Hron problem of flow over a circular cylinder with a flexible sting at the back[35] and extended for flapping fin simulations[36].

    2. Prescribe the kinematics of the fin motion from the experiments.

    3. Monitor the time history of the force production and the shape of the fin along several plane cuts throughout the flapping cycle, and compare with experiments.

Representative Results

A trapezoidal fish-inspired artificial pectoral fin was cast in two different materials (PDMS 10:1 and 20:1, both mixed with fluorescent dye) out of a mold, each with a rigid leading-edge spar inserted into the leading quarter chord (**Figure 2** and **Figure 3**). Tensile testing of the two fin materials (**Figure 3**) yielded elastic moduli of 0.38 MPa and 0.82 MPa for the PDMS 20:1 and PDMS 10:1 fins, respectively, with an R^2 of 0.99 for both measurements (see **Supplementary Figure 2** for the corresponding stress-strain curves).

To capture the motion of the fin, the camera was placed such that the micrometer-to-pixel ratio in the focused field of view was 125 µm/pixel. A delay generator was wired and programmed to trigger the laser and camera at 30 equally spaced time intervals per fin stroke based on a single trigger signal at the midpoint of each fin stroke. The fin was positioned such that the laser sheet passed through a chordwise section of the fin. This was done for eight spanwise positions from 1.876 cm to 13.132 cm from the root of the fin geometry (**Figure 2**).

For each cross-section, 200+ images were obtained for each of 30 stroke positions (phases). The programmed kinematics yielded a stroke amplitude of ±43° and a pitch amplitude of ±17° (**Figure 7A,B**). Due to the opaque rigid spar, the fin cross-section was not visible at every time step (**Figure 6**), but these occlusions were sparse and did not affect the overall 3D reconstructions. Following the image sorting, averaging, thresholding, binarization, and tracing, a 3D representation was constructed. This 3D reconstruction was compared with the results of the FSI model and the structure of a rigid fin model. The LE position in the flexible cases was assumed to be the same as that of the LE in the rigid fin for the same shape. However, the substantial reduction in the overall stiffness going from the rigid to the soft fin resulted in spanwise loading, adding a non-negligible deflection along with the LE for the present design.

Figure 7C,D illustrates these comparisons at two positions in the stroke, one in the middle of the upstroke (t = 0 s) and one in the middle of the downstroke (t = 0.567 s). The figure demonstrates the chordwise curvature induced by fluid pressure on the PDMS 10:1 fin, leading to a mean normalized chord displacement of the trailing edge at the longest chord section of displacement/chord (d/c) = 0.36

in mid upstroke and d/c = 0.33 in the mid downstroke, as measured in the experiments. This compares with d/c = 0.44 in mid upstroke and d/c = 0.39 in mid downstroke from the CFD simulations with the FSI model. The results also demonstrate some spanwise deflection along the leading edge in the experiments, which was not modeled for the simulations.

Further comparisons were made between the shape deformations of the PDMS 10:1 and PDMS 20:1 fins (**Figure 8A**). At the middle of upstroke (t = 0 s,) the trailing edge displacement at the longest chord section was measured as d/c = 0.36 for the PDMS 10:1 fin and d/c = 0.51 for the PDMS 20:1. Finally, **Figure 8B** shows the reconstructed 3D fin shapes from the PLIF, FSI, and rigid cases in the mid-upstroke (t = 0.567s). This demonstrates the capability of the present technique to provide high-fidelity validation for FSI simulations.

In addition to measurements of the deformation time-history, as detailed previously, direct measurements of thrust and mechanical power provide valuable data for analyzing fin propulsive performance. For the kinematics presented, the PDMS 10:1 fin produced a stroke averaged thrust of F_x = 0.51 N, measured with a strain gauge load cell, and an average total power of P_m = 2.38 W, measured with current and voltage sensors. Thrust and hydrodynamic power computed from the CFD simulation for the PDMS 10:1 field yielded F_x = 0.50 N and P_h = 0.49 W. The PDMS 20:1 fin produced an experimentally measured stroke averaged thrust of F_x = 0.48 N and an average power of P_m = 2.30 W. The hydrodynamic power comprised approximately 20% of the total power, while mechanical losses in the motor were a larger contributor to power consumption. As such, the differences in hydrodynamic power and efficiencies could have varied significantly between fins of different material properties, but the total power remained relatively consistent.
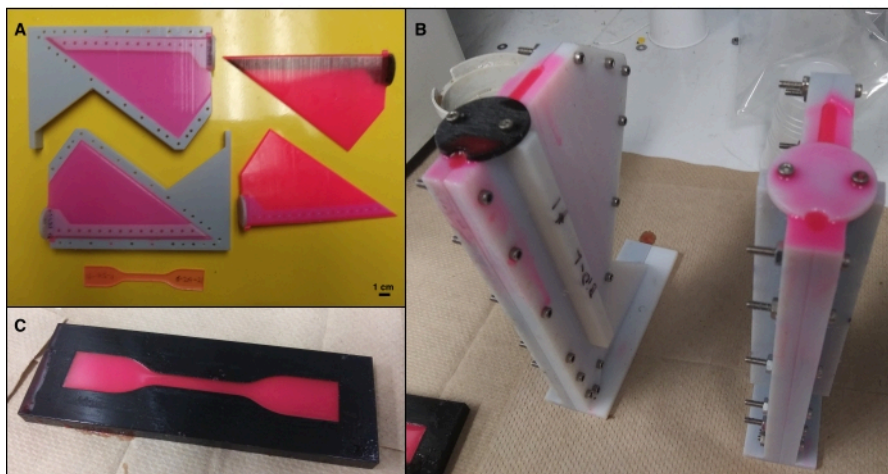

Figure 1: Custom plastic molds to cast the fins (A and B) and tensile test specimens (C). The molds and rigid spars for the fins were 3D printed in rigid plastic (black and gray), and the fins and tensile test specimens were cast from PDMS mixed with a fluorescent dye (pink). Please click here to view a larger version of this figure.
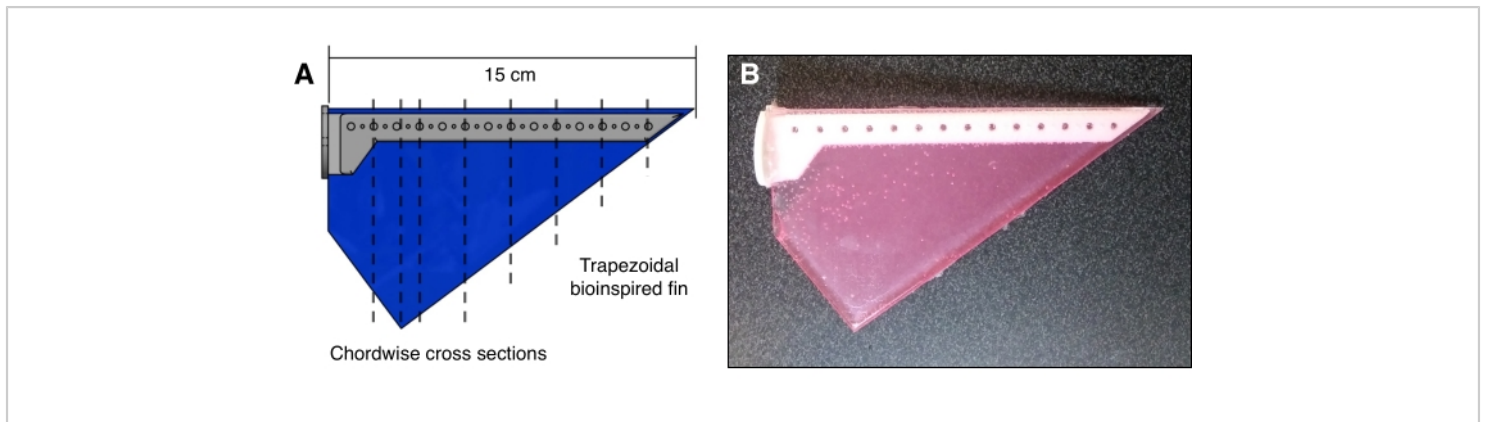
Figure 2: Bioinspired fin planform geometry used in experiments. (**A**) CAD model illustrating the rigid spar (gray) and PDMS fin (blue), with dashed black lines indicating the chordwise cross-sections used in planar laser-induced fluorescence (PLIF) experiments. (**B**) Fluorescent PDMS fin (pink) with a rigid plastic spar (white). Please click here to view a larger version of this figure.
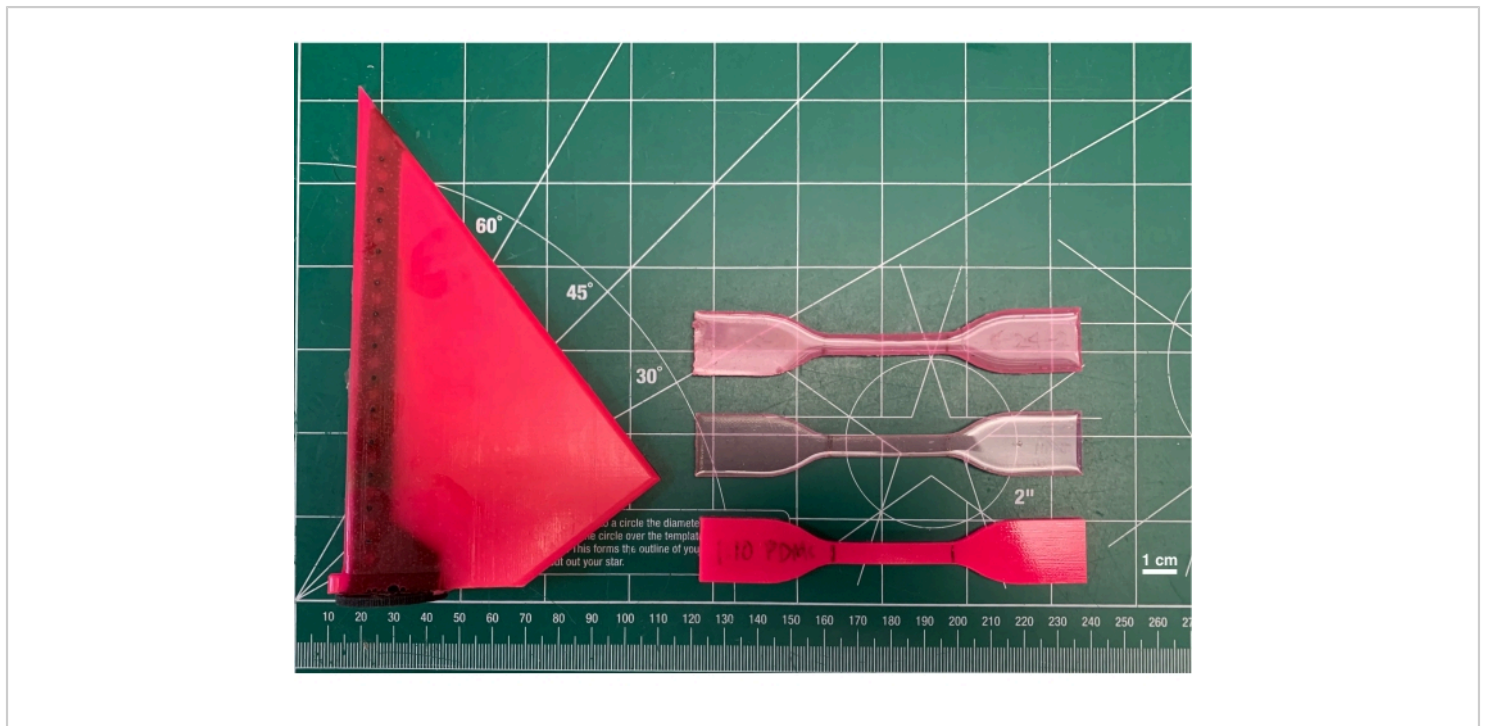

Figure 3: Example of a finished fin and tensile testing specimens. Mold-casted PDMS fin with a black rigid spar (left) and three examples of Type IV specimens (right) for tensile testing to obtain the material properties of each batch of fluorescent PDMS. Please click here to view a larger version of this figure.
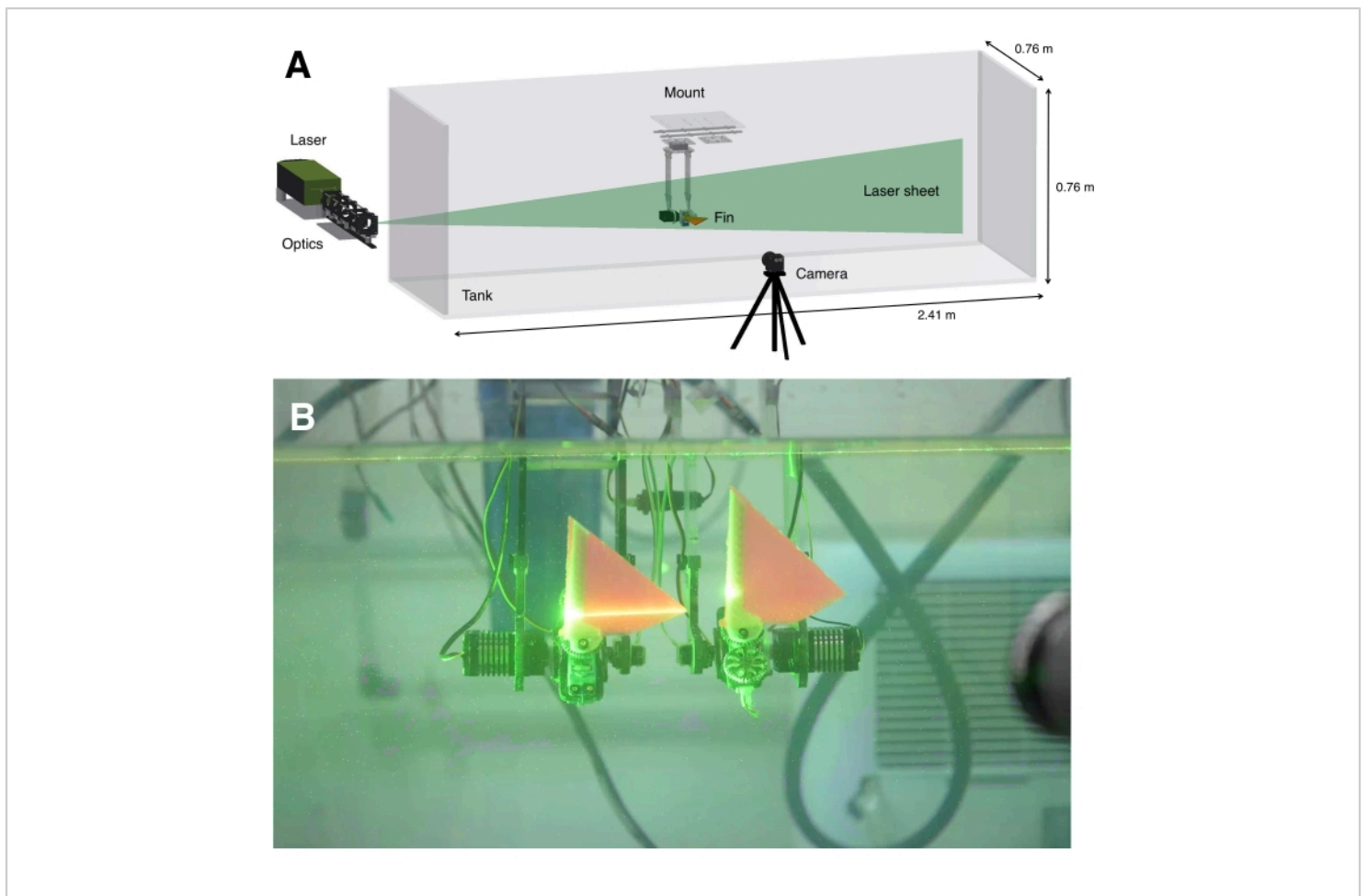
Figure 4: Experimental setup. (**A**) 3D CAD view of the experimental setup with the laser and optics, green laser sheet, tank, fin mounted to a platform, and camera. (**B**) An example image showing the mounted fins in the tank, with the laser turned on and a camera visible on the far right. Although two fins are shown in this tandem fin setup, which can obtain the kinematics for future studies of fin-fin interactions, PLIF measurements were recorded for only the front fin in this study. Furthermore, the image contains ambient light to visualize the setup, but the ambient lights were turned off during all experiments to improve the signal-to-noise ratio. Please click here to view a larger version of this figure.
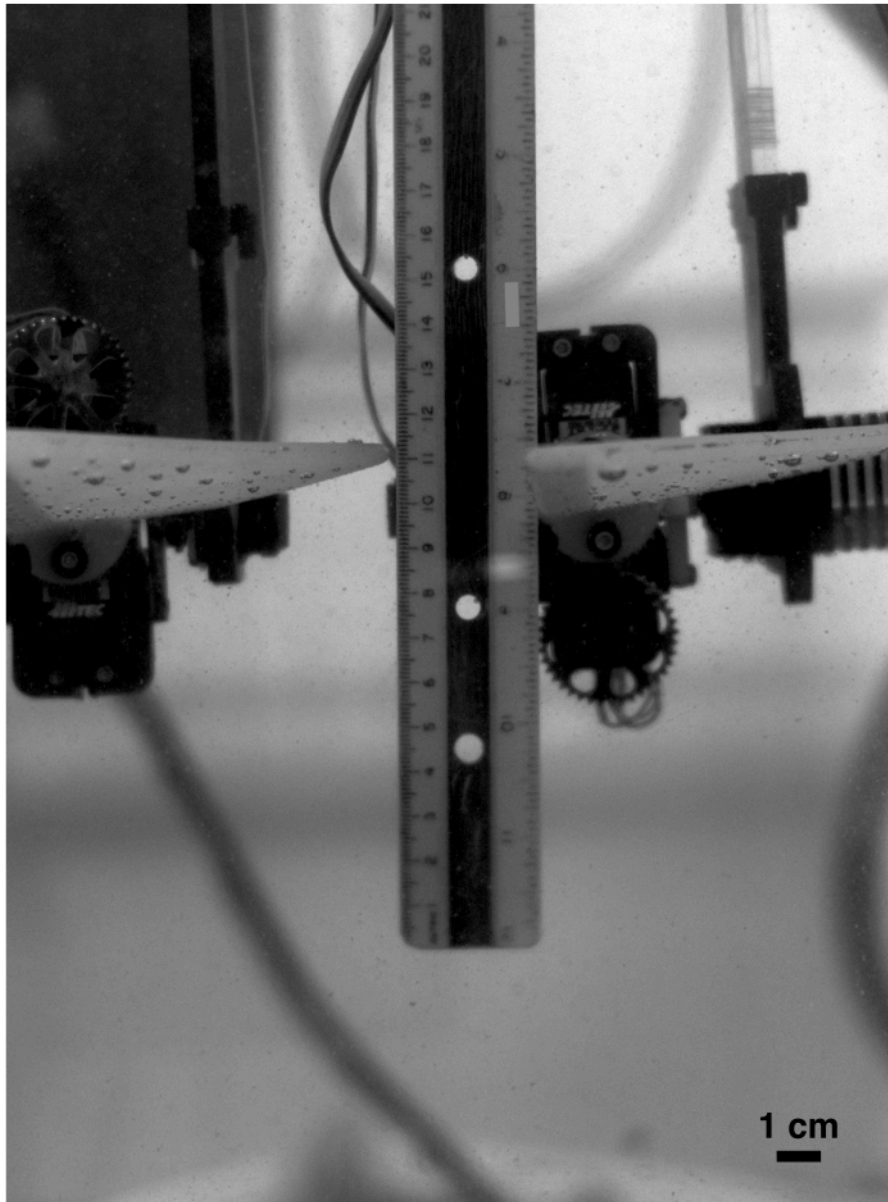
Figure 5: Calibration image. Before running the experiments, calibration images were obtained using a standard ruler to measure the micrometer-to-pixel ratio. Please click here to view a larger version of this figure.
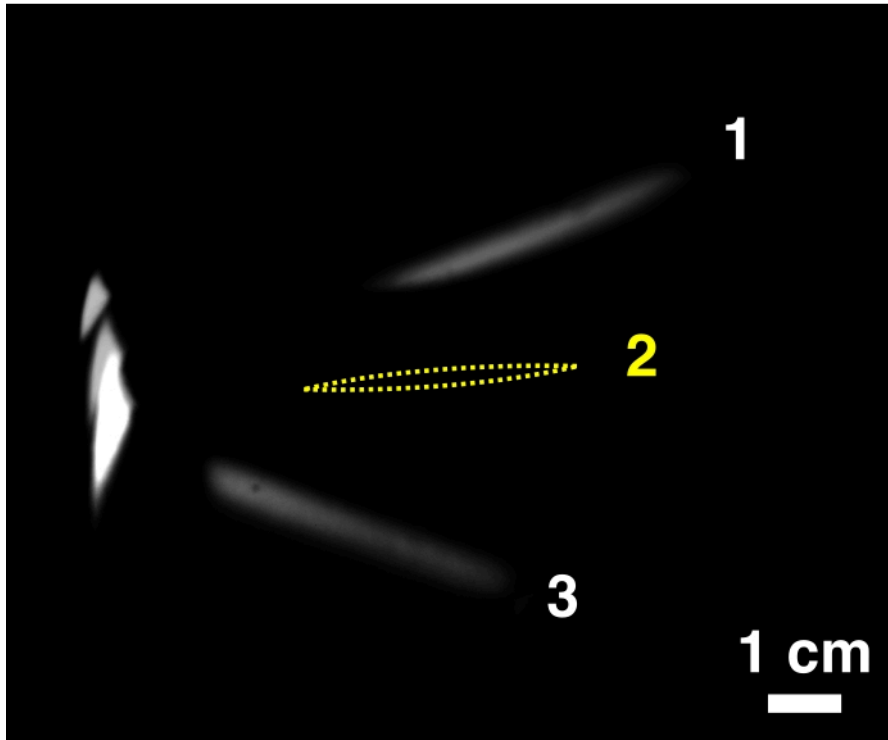
Figure 6: Fin images of three time steps overlaid, with a representative example of fin occlusion at one time step.
The fin cross-section is visible in Steps 1 and 3, whereas the opaque rigid spar occludes the fin at Step 2, where an estimate of the fin position is drawn in yellow. Please click here to view a larger version of this figure.

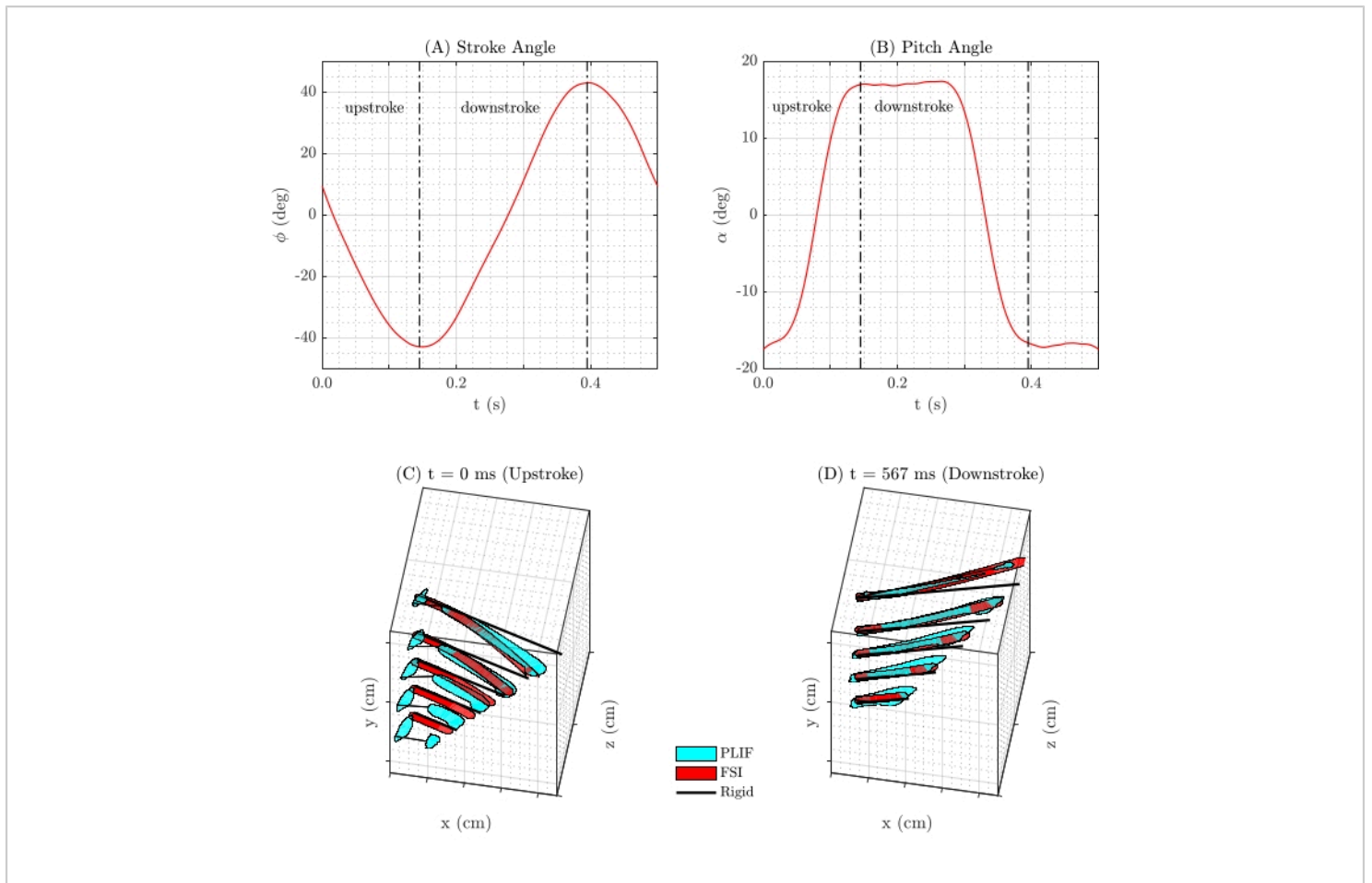**Figure 7: Fin kinematics.** (**A**) The stroke amplitude (±43°) and (**B**) pitch amplitude (±17°) of the fin kinematics over time. A comparison of the PDMS 10:1 fin (light blue), FSI data of the PDMS 10:1 fin (red), and rigid fin (black) to illustrate the difference in fin positions at two time-steps in the (**C**) upstroke and (**D**) downstroke. Please click here to view a larger version of this figure.
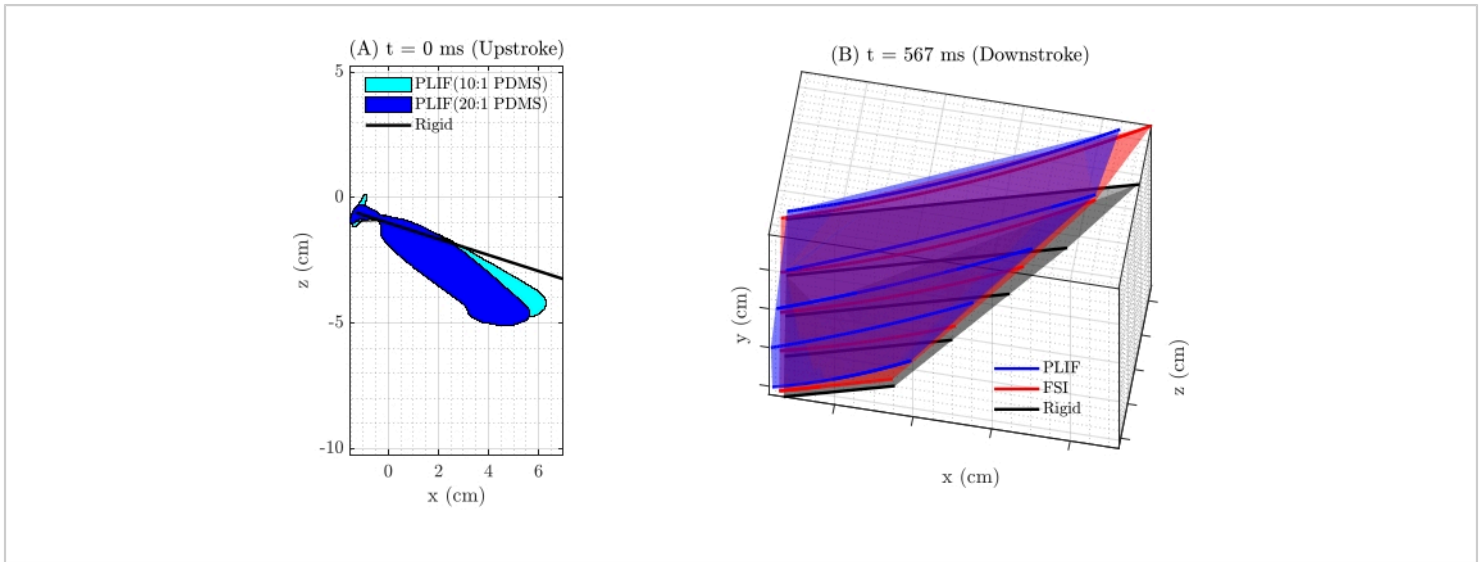
Figure 8: Comparison of fin deformation. (**A**) A comparison of the PLIF method of obtaining fin kinematics at one example time-step to demonstrate the effects of stiffness on fin deformation. The PLIF measurement for the more compliant 20:1 PDMS fin (dark blue) shows more deformation than the more rigid 10:1 PDMS fin (light blue), and both show substantial differences from a rigid fin (black). (**B**) 3D reconstructed fin shapes from the PLIF for 10:1 PDMS, FSI for 10:1 PDMS, and rigid cases at one example time-step to compare the surface fits. Please click here to view a larger version of this figure.

Supplementary Figure 1: Software interface for the delay generator. The user interfaces for software to control the delay generator, with settings to produce PLIF images at 30 Hz by coordinating the timing of the two laser heads and camera with the fin trigger. Please click here to download this File.

Supplementary Figure 2: Tensile test results for PDMS. Stress-strain curves for two mixes of PDMS (20:1, a more flexible mix with an elastic modulus of 0.38 MPa, and 10:1, a more rigid mix with an elastic modulus of 0.82 MPa). Please click here to download this File.

Supplementary Coding File 1: "Assembly2.stl" is an assembly of files to 3D print the custom fin molds. Please click here to download this File.

Supplementary Coding File 2: "SimpleFin-AR3Bio-soft-v2-fin2c.stl" is the STL file to print the fin insert, a rigid portion of the fin that serves as the attachment to the servo. Please click here to download this File.

Supplementary Coding File 3: "SimpleFin-AR3Bio-soft-v2b-moldL.stl" is the left half of the 3D print mold for the flexible fin. Please click here to download this File.

Supplementary Coding File 4: "SimpleFin-AR3Bio-soft-v2b-moldR.stl" is the right half of the 3D print mold for the flexible fin. Please click here to download this File.

Supplementary Coding File 5: "ASTM-TestPiece-Mold-v2b-TypeIV_Flat_DIN53504.stl" is the 3D print mold to create Type IV specimens for tensile testing. Please click here to download this File.

Discussion

Planar laser-induced fluorescence is typically used to visualize aqueous flows by seeding the fluid with dye, which fluoresces when exposed to a laser sheet[25,26]. However, using PLIF to visualize deformations in compliant materials has not been previously reported, and this study describes an approach for obtaining time history measurements of high-resolution shape deformation in flexible solid fins using PLIF. Comparing these fin measurements with FSI simulations validates the numerical models and provides further confidence in using computational results for fin design and control.

Among the limitations of PLIF for compliant materials, deformation characterization includes occlusion due to opaque elements in the structure (the leading-edge rigid spar in this study). Additionally, the PLIF technique is affected by total internal reflection (TIR), which occurs when the local incidence angle of the light at the PDMS-water interface exceeds the associated critical value. Although the cast PDMS fins are optically transparent, they have a much higher refractive index (1.49) than water (1.33), leading to optical distortion and occlusion with a critical angle of 63.5°. Therefore, when there is a large deformation (e.g., near the ends of the fins in the present study), the local incidence angle may exceed 63.5°. Consequently, the incident laser beam is reflected back into the fin, resulting in a much larger "fluorescent area" on the captured image, which affects the image quality and shapes detected from this technique. One method to resolve this issue for future studies is to use an optical index-matched working fluid, such as sodium iodide (NaI) solution[40]. However, this is deemed out of scope for the present study as this issue does not affect most fin cross-sections.

When optical index matching is not feasible, the concentration of fluorescent pigment during casting may be adjusted to mitigate this effect. Higher concentrations of the fluorescent dye can improve the SNR, but if there is too much pigment and the curvature (deflection) of the fin is high, the effect of the internal reflection can be too strong. This can cause image dilation for those profiles. In addition, strong considerations should be made to determine the optimum laser incidence angle with respect to the expected dominant deflection (if any) to minimize the effect of internal reflections. To illustrate, the cross-sectional profiles vary for the up and down strokes. In the latter, as the light refracted through the LE-side of the fin, it underwent multiple internal reflections at subsequent chordwise locations, making the profile shape significantly dilated. For the upstroke, the incident light did not interact with the rigid or flexible parts of the fins more than once, resulting in a crisp profile. This variation precludes a general profile mask from being algorithmically generated, as the extent of transmission and reflection varies during the stroke cycle as well. Although the image analysis considers a dynamic threshold to address this, it is still challenging to generate a cross-sectional envelope automatically.

The concave surface is more prone to internal reflections than the convex side. Hence, an alternative approach for obtaining a more accurate centerline profile was explored by offsetting the convex surface by the half-mean fin thickness. However, the resultant profile did not vary significantly compared to that obtained by the least-square fit.

Furthermore, the tensile testing and subsequent curve fitting assume a linear stress-strain relationship for small strains[39]. However, this assumption is not valid for larger deformations, affecting the calculated eigenfrequencies used as inputs to the FSI model. Efforts to obtain a more accurate FSI

prediction by accounting for such nonlinear effects are deemed out of the present scope but relevant for future studies.

Thus, this study has demonstrated the effect of fin stiffness on bioinspired robotic fins and validated the computational models. Pairing these measurements of solid deformations with the simultaneous measurement of fluid flows as described in other PLIF studies[25], future studies will improve the experimental analysis of FSI in robotic fins, bioinspired soft robots, and other applications by integrating dyes that fluoresce at various wavelengths and multiple cameras. Due to the wide use of PDMS in other research fields[24], this PLIF technique of visualizing deformations in flexible solids has the potential to benefit communities of researchers in engineering, physics, biology, and medicine.

Disclosures

The authors have nothing to disclose.

Acknowledgments

References

1. Barrett, D. S., Triantafyllou, M. S., Yue, D. K. P., Grosenbaugh, M. A., Wolfgang, M. J. Drag reduction in fish-like locomotion. *Journal of Fluid Mechanics.* **392**, 183-212 (1999).

2. Hobson, B. W., Murray, M. M., Pell, C. PilotFish: maximizing agility in an unmanned-underwater vehicle. *Proceedings of the 11th International Symposium on Unmanned Untethered Submersible Technology.* **99-8 - 01**, 41-51 (1999).

3. Licht, S., Polidoro, V., Flores, M., Hover, F. S., Triantafyllou, M. S. Design and projected performance of a flapping foil AUV. *IEEE Journal of Oceanic Engineering.* **29** (3), 786-794 (2004).

4. Zhou, C., Wang, L., Cao, Z., Wang, S., Tan, M. Design and control of biomimetic robot fish FAC-I. *Bio-mechanisms of Swimming and Flying.* 247-258 (2008).

5. Kato, N. et al. Elastic pectoral fin actuators for biomimetic underwater vehicles. *Bio-mechanisms of Swimming and Flying.* 271-282 (2008).

6. Moored, K. W., Smith, W., Hester, J. M., Chang, W., Bart-Smith, H. Investigating the thrust production of a myliobatoid-inspired oscillating wing. *Advances in Science and Technology.* **58**, 25-30 (2008).

7. Sitorus, P. E., Nazaruddin, Y. Y., Leksono, E., Budiyono, A. Design and implementation of paired pectoral fins locomotion of labriform fish applied to a fish robot. *Journal of Bionic Engineering.* **6** (1), 37-45 (2009).

8. Tangorra, J. L., Lauder, G. V., Hunter, I. W., Mittal, R., Madden, P. G. A., Bozkurttas, M. The effect of fin ray flexural rigidity on the propulsive forces generated by a biorobotic fish pectoral fin. *Journal of Experimental Biology.* **213** (23), 4043-4054 (2010).

9. Park, Y.-J., Jeong, U., Lee, J., Kim, H.-Y., Cho, K.-J. The effect of compliant joint and caudal fin in thrust generation for robotic fish. *2010 3rd IEEE RAS & EMBS*

International Conference on Biomedical Robotics and Biomechatronics. 528-533 (2010).

10. Palmisano, J. S., Geder, J. D., Ramamurti, R., Sandberg, W. C., Banahalli, R. Robotic pectoral fin thrust vectoring using weighted gait combinations. *Applied Bionics and Biomechanics.* **9**, 802985 (2012).

11. Esposito, C. J., Tangorra, J. L., Flammang, B. E., Lauder, G. V. A robotic fish caudal fin: effects of stiffness and motor program on locomotor performance. *Journal of Experimental Biology.* **215** (1), 56-67 (2012).

12. Hannard, F., Mirkhalaf, M., Ameri, A., Barthelat, F. Segmentations in fins enable large morphing amplitudes combined with high flexural stiffness for fish-inspired robotic materials. *Science Robotics.* **6** (57), eabf9710 (2021).

13. Lauder, G. V., Madden, P. G. A. Fish locomotion: kinematics and hydrodynamics of flexible foil-like fins. *Experiments in Fluids.* **43** (5), 641-653 (2007).

14. Bazaz Behbahani, S., Tan, X. Role of pectoral fin flexibility in robotic fish performance. *Journal of Nonlinear Science.* **27** (4), 1155-1181 (2017).

15. Wu, X., Zhang, X., Tian, X., Li, X., Lu, W. A review on fluid dynamics of flapping foils. *Ocean Engineering.* **195**, 106712 (2020).

16. Park, H., Park, Y.-J., Lee, B., Cho, K.-J., Choi, H. Vortical structures around a flexible oscillating panel for maximum thrust in a quiescent fluid. *Journal of Fluids and Structures.* **67**, 241-260 (2016).

17. Shinde, S. Y., Arakeri, J. H. Flexibility in flapping foil suppresses meandering of induced jet in absence of free stream. *Journal of Fluid Mechanics.* **757**, 231-250 (2014).

18. Sampath, K., Geder, J. D., Ramamurti, R., Pruessner, M. D., Koehler, R. Hydrodynamics of tandem flapping pectoral fins with varying stroke phase offsets. *Physical Review Fluids.* **5** (9), 094101 (2020).

19. Young, Y. L. Fluid-structure interaction analysis of flexible composite marine propellers. *Journal of Fluids and Structures.* **24** (6), 799-818 (2008).

20. Hughes, B., Burghardt, T. Automated visual fin identification of individual great white sharks. *International Journal of Computer Vision.* **122** (3), 542-557 (2017).

21. Watanabe, Y., Komuro, T., Ishikawa, M. 955-fps real-time shape measurement of a moving/deforming object using high-speed vision for numerous-point analysis. *Proceedings 2007 IEEE International Conference on Robotics and Automation.* 3192-3197 (2007).

22. Teng, J., Hu, C., Huang, H., Chen, M., Yang, S., Chen, H. Single-shot 3D tracking based on polarization multiplexed Fourier-phase camera. *Photonics Research.* **9** (10), 1924 (2021).

23. Zhang, B., Dong, Q., Korman, C. E., Li, Z., Zaghloul, M. E. Flexible packaging of solid-state integrated circuit chips with elastomeric microfluidics. *Scientific Reports.* **3** (1), 1098 (2013).

24. Majidi, C. Soft-matter engineering for soft robotics. *Advanced Materials Technologies.* **4** (2), 1800477 (2018).

25. *Springer Handbook of Experimental Fluid Mechanics.* Springer Berlin Heidelberg. Berlin, Heidelberg (2007).

26. Crimaldi, J. P. Planar laser induced fluorescence in aqueous flows. *Experiments in Fluids.* **44** (6), 851-863 (2008).

27. Davidson, D. F., Hanson, R. K. Spectroscopic Diagnostics. *Handbook of Shock Waves.* 741-VI (2001).

28. *Handbook of Shock Waves.* Academic Press. San Diego (2001).

29. Yang, W. J. *Handbook of Flow Visualization.* Routledge (2018).

30. Cowen, E. A., Chang, K.-A., Liao, Q. A single-camera coupled PTV-LIF technique. *Experiments in Fluids.* **31** (1), 63-73 (2001).

31. Hanson, R. K., Seitzman, J. M., Paul, P. H. Planar laser-fluorescence imaging of combustion gases. *Applied Physics B Photophysics and Laser Chemistry.* **50** (6), 441-454 (1990).

32. Houghton, I. A., Koseff, J. R., Monismith, S. G., Dabiri, J. O. Vertically migrating swimmers generate aggregation-scale eddies in a stratified column. *Nature.* **556** (7702), 497-500 (2018).

33. Mohaghar, M., Webster, D. R. Characterization of non-linear internal waves using PIV/PLIF techniques. *14th International Symposium on Particle Image Velocimetry.* **1** (1) (2021).

34. Yue, Y., Zhang, H., Zhang, Z., Chen, Y. Tensile properties of fumed silica filled polydimethylsiloxane networks. *Composites Part A: Applied Science and Manufacturing.* **54**, 20-27 (2013).

35. Ramamurti, R., Geder, J., Viswanath, K., Lohner, R., Soto, O. *Coupled CFD, structure and control tool for simulation of flapping wing analysis.* (2019).

36. Geder, J. D., Ramamurti, R., Sampath, K., Pruessner, M., Viswanath, K. Fluid-structure modeling and the effects of passively deforming fins in flapping propulsion systems. *OCEANS 2021: San Diego - Porto.* 1-9 (2021).

37. Anderson, D. A., Tannehill, J. C., Pletcher, R. H., Ramakanth, M., Shankar, V. *Computational Fluid Mechanics and Heat Transfer.* CRC Press. Fourth edition. | Boca Raton, FL : CRC Press, 2020. | Series: Computational and physical processes in mechanics and thermal sciences. (2020).

38. Löhner, R. *Applied Computational Fluid Dynamics Techniques: An Introduction Based on Finite Element Methods.* John Wiley & Sons. Chichester, England; Hoboken, NJ (2008).

39. D20 Committee. *Test Method for Tensile Properties of Plastics.* ASTM International. (2022).

40. Bai, K., Katz, J. On the refractive index of sodium iodide solutions for index matching in PIV. *Experiments in Fluids.* **55** (4), 1704 (2014).